IEEE Transactions on Geoscience
and Remote Sensing

Operational Atmospheric Correction for Imaging Spectrometers Accounting for the Smile Effect

scholarONE™
Manuscript Central

Operational Atmospheric Correction for Imaging Spectrometers Accounting for the Smile Effect

Rudolf Richter, Daniel Schläpfer, and Andreas Müller

Abstract

Hyperspectral pushbroom imagers are affected by a number of artifacts, such as pixel-nonuniformity, spectral smile, and keystone. These have to be taken into account during system-correction, ortho-rectification, or atmospheric correction, as performed in processing and archiving facilities (PAFs). This contribution is presenting an efficient and accurate smile correction method integrated in the atmospheric correction. The proposed technique will be used in the PAF of the German hyperspectral EnMAP mission. The spectral smile shift across the detector array is parametrized with a 4th order polynomial function for each spectral band based on the instrument optical design model or measured laboratory data. Alternatively, spectral smile shifts can be calculated from image data using signatures of atmospheric absorption regions.

The concept for the time-optimized processor is outlined and results are presented for simulated EnMAP data and existing pushbroom imagery (Hyperion, AISA, HySpex).

Index Terms

Pushbroom imaging spectrometer, smile, water vapor, surface reflectance, EnMAP.

I. INTRODUCTION

The operational fully automatic processing of hyperspectral pushbroom imagery from level 0 (raw data) to level 2 (L2, surface reflectance) is a challenging task, because many instrument-specific artifacts such as pixel non-uniformity, spectro-radiometric and geometric calibration have to be accounted for [1] - [5]. An important artifact for most pushbroom hyperspectral imagers is the spectral "smile", also known as spectral non-uniformity or spectral misregistration. It is a consequence of optical aberrations that cause the spectrometer entrance slit, representing the across-track swath, to be projected as a curve on the rectilinear detector array [6], [8]. Thus, the center wavelength of each spectrometer channel varies in across-track direction. Reference [6] proposed to correct this effect during the atmospheric correction. The problem is a very large processing time, because an image column loop is needed in addition to the channel loop during atmospheric correction, because each channel in itself is a "spectrometer" in

1

column direction. Once the pushbroom artifacts have been removed the full potential utility of hyperspectral images can be exploited as specified by user information requirements [7].

This contribution presents an efficient and accurate smile correction algorithm as an integral part of the atmospheric correction. It is designed, implemented, and validated in the frame of the German hyperspectral EnMAP mission, but the method is generally applicable to data from pushbroom imaging spectrometers. It is fully automatic making it suitable for L2 processors in processing and archiving facilities [13].

EnMAP covers the spectral region 420 - 2450 nm with 245 channels and bandwidths between 6 and 12 nm. It is based on a prism design with two spectrometers (VNIR: 420 - 1000 nm; SWIR: 900 - 2450 nm). Spectral smile is specified to be smaller than 0.2 pixel. The radiometric resolution is 14 bits. The spatial resolution is 30 m and the nadir swath width is 30 km with an off-nadir across-track tilt capability of 30°. Scenes are acquired from a sun-sunchronous 643 km orbit with a revisit time of 23 days at ±5° off-nadir angles and 4 days at ±30°, and a local time of equator crossing at 11 h [9]. The instrument will be manufactured by an industrial consortium with Kayser-Threde [10] as prime contractor.

The paper is structured as follows: section II presents the atmospheric correction method accounting for the channel-dependent smile parameters. These are usually derived from the optical design model or from measured laboratory data. Since the instrument performance might change in an airborne or spaceborne environment, additional checks of the spectral behavior are required during the mission. For this purpose, some instruments are equipped with spectral calibration devices, e.g., MERIS [11] and APEX [12], [13]. However, the majority of instruments do not possess a calibration panel because of space, mass, and cost restrictions. In any case, a check of the spectral calibration, and if necessary a re-calibration, is possible with an analysis of atmospheric absorption features in the image cube [14], [15]. This approach is part of the proposed off-line calibration (section III) and can even be conducted for instruments with a spectral calibration panel [11]. Section IV presents validation results for simulated EnMAP top-of-atmosphere radiance cubes as well as data recorded with existing airborne and spaceborne sensors. The last sections contain a discussion and conclusion.

II. METHOD OF ATMOSPHERIC CORRECTION ACCOUNTING FOR SMILE

The general mathematical background of atmospheric correction (AC) using a look-up table (LUT) approach for the inversion problem and a radiative transfer code is well known [6], [16] - [22]. However, only few contributions address issues relevant to an operational L2 processing which is the subject of this paper. As AC techniques are well documented in the literature we will restrict the discussion to items related to an efficient processing of the smile correction. Here, the calculation of the radiative transfer in the earth's atmosphere is conducted with the MODTRAN4 code [23], [24].

The presented approach is implemented in the ATCOR model [25], [26] available from ReSe (http://www.rese.ch/).

2

A. Optimized smile processor

Fig. 1 presents a flow chart of the optimized smile processor. It consists of three main blocks labeled (A), (B), (C). Block (A) contains the high spectral resolution (0.6 nm) database Y_0 of LUTs which currently are generated with MODTRAN4. The Y_0 represents all radiative transfer functions for a discrete 6-D parameter space, see Table III in section IV-A for an example. Y_0 comprises the six radiative transfer functions required for a surface reflectance retrieval, i.e., path radiance, direct and diffuse transmittance, direct and diffuse solar flux, and spherical albedo [20], [21]. The database Y_0 has to be interpolated for the parameters of the scene to be processed, i.e., for the pertaining solar and viewing geometry, ground elevation, and aerosol model. The interpolated database is Y, still at the original 0.6 nm resolution. Then the convolution with the spectral response function R_k of channel k has to be performed resulting in an adapted data base Y_k. R_k consists of two components, the $R_k(\lambda)$ containing the form of the filter function, and the smile shift function $P_k(j)$ describing the shift of the center wavelength as a function of the detector column number j. In our definition $R_k(\lambda)$ defines the channel filter curve for the center of the detector array, and $P_k(j)$ is defined as a 4th-order polynomial. It specifies the spectral smile shift with respect to the center of the detector array

$$P_k(j) = \sum_{i=0}^{4} a_i^{(k)} \cdot j^i \tag{1}$$

where $a_i^{(k)}$ are the polynomial coefficients, j is the across-track pixel number (ranging from 1 to n), and $P_k(n/2) = 0$. In other words, the spectral response function at the detector column j is defined as

$$R_k(\lambda, j) = R_k(\lambda) + P_k(j) \tag{2}$$

This means the center wavelength of the response function is shifted but the shape is assumed to be the same. If the detector array is centered on the optical axis a second order polynomial is already sufficient [15], but the use of a 4th-order polynomial offers more flexibility, i.e., it can account for rotational misalignments and other effects. Also, a polynomial is preferred as it describes the curvature as produced by the optics better than an arbitrary interpolation of data points. Thus, eq.'s 1, 2 are accurate for all practical purposes. However, if necessary, a change in bandwidth $B_k(\lambda)$ with column number can also be taken into account

$$B_k(\lambda, j) = B_k(\lambda) + Q_k(j) \tag{3}$$

where $B_k(n/2) = 0$ and $Q_k(j)$ is another 4th-order polynomial.

As all Y_k functions are required for the surface reflectance retrieval (block C) and a part is also needed for the calculation of the water vapor map (block B) the functions are calculated once and stored for the remaining session. The Y_k's depend on the water vapor column (WVC) and aerosol optical thickness (AOT) parameters, as well as solar and viewing geometry, and ground elevation. For brevity, only the dependence on WVC and AOT is indicated.

Block (B) sketches the per-column water vapor algorithm, in our case we use the enhanced APDA method [27] with adaptations for the smile effect as described in the next subsection. After finishing the column loop j, the

3

vectors $W(j)$ with the water vapor values for all pixels are arranged in the image map $W(x, y)$. Block (C) sketches the channel and column loops for the surface reflectance retrieval. Again, when the column loop j terminates, the vectors $\rho_k(j)$ are arranged in the map $\rho(x, y, k)$ for channel k. The surface reflectance cube $\rho(x, y, *)$ is obtained after completing the channel loop.

Some points are important for an efficient processing in a matrix-oriented coding such as IDL and Matlab: first the smile-influenced atmospheric correction database functions Y_k are needed during the per-column water vapor retrieval as well as later, so they are stored in memory and in a file after the first calculation. Secondly, the Y_k's are only calculated for those columns for which the difference in smile shift between successive columns (eq. 1) exceeds a certain threshold T (we use T=0.02 nm). Therefore the number of column loops generally varies with wavelength or channel number as each channel has its own smile shift function. Third, the column loop is not applied to those channels where the five smile polynomial coefficients are all zero. Instead, in a matrix oriented coding language, a much faster execution is achieved using matrix algebra and avoiding column loops. This feature can be used to reduce the processing time by about 30% by setting all smile coefficients to zero for channels in atmospheric window regions.

Table I shows an example of relative processing times for the EnMAP spectrometer with 245 channels, 118 of which are located in atmospheric absorption regions. The relative time is set to 1 in case of a processing without smile correction. If smile is characterized and considered for all channels, the relative time increases by a factor of 6. If smile is only considered for the 118 channels affected by absorption (still with all channels being processed) the relative time factor is 4.2. The time saving for the reduced set of channels with optimized smile correction is not a factor of 2, because the overall processing comprises not only the surface reflectance retrieval, but also the calculation of land, water, cloud masks, as well as aerosol and water vapor maps. The 'brute force' correction in this table refers to a simple column loop for the spectral smile in addition to the channel loop where all processing optimizations summarized in Fig. 1 are missing. And last but not least, if Y_k functions are stored in a file, a faster re-processing can be conducted, e.g., with a different set of bands for the water vapor algorithm.

B. Changes in APDA algorithm for smile sensors

Automatic water vapor retrieval from imaging spectroscopy data is a crucial part of any atmospheric correction procedure, as almost half of the wavelength range between 400 and 2500 nm is affected by water vapor absorptions. Common methods such as the herein used atmospheric precorrected differential absorption method APDA [27] rely on the water vapor absorption features around 940 and 1130 nm. The method analyzes the absorption depth under consideration of the path scattered radiance component. As the absorption features exhibit sharp edges in absorption, wavelength shifts in a range of 0.1 nm to 0.2 nm can already lead to significant differences in the measured signal in case of very narrow channel bandwidths and strong absorption features. Thus, the smile correction is of high relevance for a correct retrieval of the atmospheric water vapor.

4

The procedure is adapted to the characteristics of a system affected by spectral smile. A first guess water vapor map is first retrieved using the average band characteristics, without considering smile. This map is then used in a second iteration of processing in order to obtain an approximated path radiance term which is later subtracted from the at-sensor radiance values. The second iteration is done on a per-column basis: for each image column, a column specific LUT is derived using the information about the spectral position of the bands at this column. The APDA method is then applied using the pre-selected spectral bands on one column only. After the processing, the derived per-column LUTs are stored in a binary file for optional later use with different spectral bands or aerosol contents. Finally, the water vapor map is smoothed by a user-defined distance in order to remove artifacts over small dark targets.

III. Retrieval of smile parameters from the imagery

Initially, the smile characterization for each spectrometer channel is derived from laboratory measurements or an optical design model. From such data, the wavelength shift with respect to the center pixel of the detector array can be parametrized using a polynomial fit (see section II-A). A 4th order polynomial provides an accurate fit ($<$ 0.01 nm) for the EnMAP optical design model. For other typical pushbroom sensors a 2nd or 3rd order polynomial fit is already sufficient [15]. The selected polynomial order plays a negligible role for the processing time of the image cube. In case of instrument changes during the mission, a spectral re-calibration might be necessary from the image data or from onboard calibration facilities using well-defined absorption features. Onboard spectral calibration devices such as interference or rare earth filters would be well suited for this purpose [11], [12]. However, such devices are often not available in sensor systems. Atmospheric gas absorption features or solar Fraunhofer lines have been taken as a reference from the imagery itself. The principal method was already described in several papers [14], [29], [15]. Some processing steps are common to all variants of the method, namely the use of calibrated image data, the column-averaging of the image, the calculation of a set of spectrally shifted reference radiances, and a merit function to be minimized. We propose an off-line approach to derive the 4th order polynomial smile fit coefficients for appropriate channels in atmospheric absorption regions. The method itself is automatic by checking the spectral coverage of the instrument, spectral sampling distance, and channel bandwidths versus the position and widths of the spectral features in Table II. In addition, a manual selection of bands can be done from the potential absorption features in Table II.

The smile detection algorithm uses the following procedure:

1) A calibrated image is averaged in along track direction, leading to a signature image of the size of the detector array.
2) The surface reflectance is calculated (atmospheric correction) and smoothed.
3) The spectral bands within the spectral matching range are selected.
4) Spectral shifts with selectable intervals between 0.01-0.05 nm are calculated and applied to the selected spectral band response functions.

5

5) An appropriate pre-calculated fine-spectral resolution atmospheric LUT is selected which serves for the calculation of at-sensor radiance values for the series of spectrally shifted response functions using the average surface reflectance spectrum from step (2).

6) The derived spectral signatures are correlated to the observed column-averaged signal in the image, such that the best fitting spectral shift $\Delta\lambda_j = \Delta_j$ can be found for each image column j, i.e., the Δ_j with the highest Pearson's correlation coefficient is selected. This is equivalent to minimizing the merit function

$$\chi^2(\Delta_j) = \sum_{\Delta_j = \lambda_k - 5nm}^{\lambda_k + 5nm} \left[L_I(j,k) - L_R(\lambda_k + \Delta_j, k) \right]^2, \tag{4}$$

where $L_I(j,k)$ is the average at-sensor radiance of the image for column j and channel k, and $L_R(\lambda_k + \Delta_j, k)$ is the corresponding reference radiance for a wavelength shift Δ_j within a 5 nm interval around λ_k.

7) Image columns where no best fit can be found within the wavelength range are excluded from further analysis. A spectral feature with less than a fixed number of valid calculation points (e.g., 10 or 100) in across-track direction is excluded completely.

8) A 4th order polynomial is fitted through the remaining calculated spectral points and the respective polynomial parameters of eq. 1 are stored.

9) The polynomial parameters are interpolated and optionally extrapolated to all other bands within the same detector or spectrometer unit. Optionally, the polynomial coefficients can be set to zero in atmospheric window regions to expedite the processing (see Table I).

Once the coefficients have been determined, they are stored as sensor description parameters for a subsequent fully automatic radiometric and atmospheric processing. The proposed processor itself (section II) takes the provided polynomial functions without knowledge of the origin (laboratory, optical design model, or atmospheric features). Therefore, the most accurate option or combination of options should be selected during system validation.

IV. RESULTS OF VALIDATION

The proposed approach is validated with synthetic data of EnMAP by comparing the retrieval results (water vapor, surface reflectance) to the known input parameters, and with 'real world' data of some airborne and spaceborne instruments.

A. Simulated EnMAP cubes

In the framework of the German EnMAP mission two hyperspectral simulation tools were developed to enable a forward top-of-atmosphere (TOA) radiance simulation of image cubes containing typical pushbroom artifacts: a spectro-radiometric simulator at DLR using a small number of surface reflectance spectra, and a combined spectro-radiometric plus geometric simulator at GFZ based on natural scenes previously acquired from spaceborne and airborne instruments [9]. The purpose of these simulators is the generation of TOA radiance cubes to test the accuracy and sensitivity of the retrieval algorithm (water vapor, surface reflectance) as a function of solar geometry,

6

atmospheric conditions, and sensor parameters (center wavelengths, bandwidths, smile, noise).

Fig. 2 shows the three main components of the DLR simulator: (i) spectral libraries containing high resolution surface reflectance spectra, (ii) atmospheric parameters to calculate the radiative transfer using the MODTRAN4 code, and (iii) instrument effects specifying the spectral response functions, smile characteristics, detector linearity, and noise. The radiative transfer calculations are performed with high spectral resolutions (1 cm^{-1} in atmospheric absorption regions using the correlated k (CK) algorithm [23], 5 cm^{-1} in window regions). Finally, a LUT database with a constant spectral sampling interval of 0.6 nm is generated. These calculations are then spectrally resampled with the channel response functions, and (in case of EnMAP) a TOA radiance cube is generated for two spectrometers (VNIR and SWIR) with overlapping channels in the 900 - 1000 nm region (see Fig. 3). Due to the prism design of EnMAP the spectral bandwidth (FWHM = full width at half max) varies about 2 nm across each spectrometer [28].

Table III summarizes the parameters of the employed 6-dimensional LUT with its grid points. VZA, SZA, RAA, ELEV, VIS, and CWV denote view zenith angle, solar zenith angle, relative azimuth angle (between line-of-sight and solar azimuth), surface elevation above sea level, visibility, and columnar water vapor, respectively. VZA is covers the interval 0 to 30° as the maximum tilt angle of EnMAP is 30°. The forward simulation of the generation of the TOA radiance cubes is always performed in such a way that a multi-dimensional LUT interpolation is necessary during the retrieval in order to include LUT interpolation effects.

Following this approach and the optimized processing concept of section II, the atmospheric correction was conducted on a large number of hyperspectral TOA cubes varying the solar and viewing geometry, ground elevation, atmospheric parameters, and sensor noise level using the midlatitude summer atmosphere of MODTRAN4, a rural aerosol with a visibility of 16.3 km (AOT(550nm) = 0.44 at sea level), elevations from 0.1 to 2 km, and a 643 km orbit height. Maximum smile shifts of 2 nm and 1 nm are taken for the VNIR and SWIR spectrometers, respectively, allowing a small margin with respect to the optical instrument design model of the manufacturer. The shifts are zero at the image center and are accurately described (< 0.01 nm) by a 4th-order polynomial function. As the most important parameters with respect to the smile influence are the solar geometry, noise, and water vapor column, we present results selected accordingly.

The selected artificial test scene content consists of different vegetation types (alfalfa, conifers), soils, plastic (polyethylene), and constant reflectance surfaces. Fig. 4 shows selected results of the surface reflectance retrievals for moderate and high solar zenith angles (35.3°, 58°), medium to high water vapor columns (2.3 - 4.5 cm), and different noise levels (noise-free, SNR=200, SNR=100). The noise-free case (Fig. 4(a)) also includes a comparison without smile correction. In the investigated cases, the water vapor maps are retrieved with a relative accuracy of 5%. The accuracy in retrieved surface reflectance values is ±0.02 units for SNR = 100, and ±0.01 for SNR = 200, excluding the strong absorption regions around 1400 nm and 1800 nm. The results demonstrate that the proposed method successfully eliminates smile-induced artifacts. Of course, small residuals may occur depending on the noise

7

level. High-quality surface reflectance retrievals are obtained for $SNR = 100$. At levels around $SNR = 200$ or better the quality of the reflectance spectra is hardly discernable from the original surface reflectance spectra, so that there is no need for spectral polishing, provided the radiometric calibration is very accurate.

For EnMAP there will be a laboratory-based spectral smile characterization and an on-board spectralon doped sphere is also available. Therefore, an accurate description of the smile polynomial functions can be expected and this approach is taken in the calculation of the results presented in Fig. 4. Additionally, the simulated EnMAP TOA radiance cubes are also suitable to test the performance of the retrieval of smile parameters from the image (the concept proposed in section III). The retrieved smile parameters are then compared to the known original values used in the forward simulation. The algorithm calculates the column means of any calibrated scene and compares them to reference values obtained by shifting and convolving the channel filter functions in steps of 0.01 nm within a wavelength region, as described in section III above.

An intercomparison plot of the retrieved results is given in Fig. 5. It can be shown that the agreement of the absolute center wavelength position ranges between 0.1 nm and 0.7 nm, depending on the selected feature. The feature at 2008 nm is apparently not suitable for this type of sensor due to restrictions of the spectral resolution; further limitations are visible for 1464, 2008, 2061, and 2413 nm - these wavelengths are apparently at the criticial limit of sensitivity for the EnMAP system. The lower sensitivity of the method at longer wavelengths is mainly caused by the moderate spectral resolution (about 10 nm) of the EnMAP system at these wavelengths. The most accurate smile retrievals are obtained at 766 nm (EnMAP VNIR spectrometer) and 990 nm (VNIR and SWIR spectrometer overlap region). The shape of the smile is well retrieved for most of the features. In any case, for operational processing only well-fitting features are finally selected for a scene-based smile retrieval combined with the smile results from the doped spectralon sphere, as one wants to avoid the introduction of additional artifacts in the image.

B. Water vapor retrieval accounting for the smile effect

Another artificial scene has been created for the evaluation of the smile-considering water vapor retrieval procedure. It consists of eight selected reference spectra which have been arranged in a scene-like configuration, such that each object expands in across track direction from nadir to off-nadir positions (compare Fig. 6). At-sensor radiances have then be calculated with MODTRAN4 using the EnMAP sensor model as described above, including a simulated smile effect (2 nm in the VNIR, 1 nm in the SWIR spectrometer). The water vapor distribution has then been retrieved from this scene in four configurations based on the APDA technique and the results are depicted in Fig. 6. The first configuration calculated the water vapor without consideration of the smile effect, taking the nadir spectral response function only. An underestimation of the amount of water vapor up to 20% resulted from this configuration in smile-affected parts of the scene. Secondly, the TOA radiance data was spectrally interpolated to consistent band positions, under consideration of the smile. This linear interpolation did not improve the results

8

significantly, as interpolation is a cause of further information loss in the spectra. In the next step, a column-wise water vapor retrieval was applied as described in section II-B above. The across-track variations of the retrieved water vapor are removed by this method. However, some variations due to the non-linear reflectance spectra are still visible, yielding relative water vapor retrieval errors up to 5%. The overestimations are due to the liquid water absorption in vegetation. A last tentative improvement is achieved by applying an empirical correction for vegetation spectra, based on the NDVI value, which results are depicted in the lower right image of Fig. 6. Relative retrieval errors are then reduced to about 2%, but the underlying method for vegetation liquid water correction is not yet stable enough to apply it for operational use and needs further research.

C. Results on real data

Laboratory characterization of the spectral smile is seldom available, but even if it exists it might change during the lifetime of a mission and a re-calibration is then necessary. Since only few instruments are equipped with doped spectral panels or spheres, smile detection and correction methods have to use atmospheric features inherent in at-sensor image cubes. Therefore, we have tested our method on airborne (AISA, HySpex) and spaceborne (Hyperion) data. Results for the most suitable spectral bands at 760 and 820 nm (and 430 nm for HySpex) are given in Fig. 7. The analysis revealed minor smile effects of 0.2 nm for the HySpex system. Due to the low smile values and the moderate atmospheric absorption features the atmospheric correction of this airborne data set did not significantly improve if the smile-including approach is applied. For the AISA Eagle system with its spectral sampling interval of 2.3 nm, smile shifts up to 0.5 nm were observed. In this case, a smile correction leads to improved surface reflectance spectra in the 760 nm and 940 nm spectral regions, see Fig. 8, showing two examples of vegetation and soil spectra taken from the scene. The remaining smaller spikes are most probably caused by slight radiometric calibration uncertainties or residual inaccuracies of the radiative transfer calculations. No attempt for a re-calibration or spectral polishing was performed for this demonstration. In our cases, the accuracy of the smile retrieval was 0.1 nm to 0.4 nm, varying between images from the same sensor taken at different acquisition dates. The error depends on the available absorption features, i.e., the spectral coverage of the instrument, on the spectrometer sampling distance and bandwidth, and for airborne systems on the flight altitude which influences the absorption depth.

For Hyperion, a much stronger smile of about 3 nm is calculated in the VNIR spectrometer (Fig. 7(c)) which is in agreement with literature [8], [30]. Therefore, a smile-accounting atmospheric correction will obtain more accurate reflectance spectra, especially in atmospheric absorption regions where spikes are eliminated or at least reduced in amplitude (see Fig.'s 4(a), 8, and [6]). Note that no significant differences to the already published smile detection methods are expected as the basic assumptions are similar.

V. DISCUSSION

The first part of the methodology describes an efficient algorithm for matrix oriented languages to account for the spectral smile effect during atmospheric correction. The method reduces the processing time by a factor of 11 compared to the 'brute force' approach which simply applies an additional column loop (i.e., spectral loop

9

accounting for smile but without the optimizations described in Fig. 1) to each channel. The spectral smile shift across the detector array is parametrized with a 4th order polynomial for each channel. In atmospheric window regions the smile effect may optionally be neglected to save some processing time. Channels in the very strong atmospheric absorption regions around 1400 nm and 1800 nm are usually not processed because the signal is very low and noise dominates. For these channels a non-linear interpolation with the neighboring window channels is applied. The polynomial functions per channel can be derived from a fit with data of the optical design model of the instrument or from measured laboratory data. Another possibility is the derivation of these functions from the image cube exploiting atmospheric absorption features. The proposed operational atmospheric correction accounting for the smile effect uses polynomial functions evaluated off-line and the most accurate available option (optical design model, laboratory measurements, atmospheric features) or combination of options should be employed.

The second part of the methodology describes the retrieval of smile parameters from terrestrial or solar atmospheric absorption features in the image cube. The algorithm employs a radiative transfer code (MODTRAN4) to calculate a series of spectrally shifted reference radiances from which the smile parameters are derived. Therefore, results depend on the accuracy of the MODTRAN code. The method does not work for water surfaces because of the low signal-to-noise ratio, so it should only be applied to land scenes. As oxygen is a uniformly mixed gas in the atmosphere, the narrow oxygen-A absorption feature is especially suited to calculate the smile parameters. Here, the accuracy of the smile shift is about 0.1 nm to 0.2 nm. Water vapor features can also be employed provided there are no large variations in the scene. Here, the accuracy of the smile shift ranges between 0.2 nm to 0.7 nm (for instruments with 8 - 10 nm bandwidths) depending on the width and gradient of the atmospheric absorption feature. The algorithm does not need ground reflectance measurements to derive the wavelength shift parameters, but relies only on measured at-sensor radiance data. Therefore, it depends on the radiometric calibration of the instrument, similar to other techniques [14], [15], [29].

The retrieval of smile parameters from absorption features in the image can only be conducted for a discrete set of channels in appropriate spectral regions. A problem exists for the spectral channel interpolation or extrapolation of smile parameters. The best approach is a combination of the scene-based smile retrieval (plus the use of an on-board spectral calibration device if existing) with a sensor model of the instrument spectral dispersion law to achieve the most accurate results. In case of EnMAP, the dispersion law of the optical sensor model recommends a second order polynomial for the inter-channel interpolation which is accurate to 0.5 nm fulfilling the requirement of 0.2 pixel. This interpolation polynomial has to be distinguished from the required 4th order polynomial that describes the across-track smile variation within each channel.

VI. CONCLUSION

An efficient and accurate atmospheric correction method for smile-affected pushbroom imagery has been presented. All time-critical parts of the method are discussed with emphasis on matrix-oriented languages (IDL, Matlab).

10

Additionally, for instruments without on-board spectral calibration, a scene-based approach for the retrieval of spectral smile parameters from atmospheric absorption features has been introduced to support an update of smile parameters resulting from changes in the instrument performance during a mission. Both methods were validated with simulated hyperspectral data (spaceborne EnMAP) and real-world data from airborne and satellite spectrometers. During the EnMAP mission a spectral smile detection and characterization is planned once per month using the on-board spectral sphere and integrating sphere as well as atmospheric absorption features from EnMAP image cubes. Additional validation efforts with simultaneous ground truth measurements will be conducted.

Limitations of the smile detection and smile-based correction exist if uncertainties in radiometric calibration are present or if the spectral resolution of the instrument is not able to resolve reference spectral absorption features accurately enough. The presented methods are generally applicable for the level-2 processing of pushbroom imagery and are now candidates for use in operational processing chains of up-to-date imaging spectroscopy systems such as EnMAP, APEX, AISA Eagle, or HySpex.

11

REFERENCES

[1] P. Mouroulis, R. O. Green, and T. G. Chrien, "Design of pushbroom imaging spectrometers for optimum recovery of spectroscopic and spatial information", *Applied Optics*, vol. 39, pp.2210-2220, 2000.

[2] D. Schläpfer, J. Nieke and K. I. Itten, "Spatial PSF nonuniformity effects in airborne imaging spectrometer data", *IEEE TGRS*, vol. 45, pp.458-468, 2007.

[3] F. Dell'Endice, J. Nieke, D. Schläpfer, and K. I. Itten, "Scene-based method for spatial misregristration detection in hyperspectral imagery", *Applied Optics.*, vol. 46, pp.2803-2816, 2007.

[4] J. Nieke, D. Schläpfer, F. DellEndice, J. Brazile and K. I. Itten, "Uniformity of Imaging Spectrometry Data Products", *IEEE TGRS*, vol. 46, pp.3326-3336, 2008.

[5] A. Dadon, E. Ben-Dor, and A. Karnieli, "Use of derivative calculations and minimum noise fraction transform for detecting and correcting spectral curvature effect (Smile) in hyperion images", *IEEE TGRS*, vol. 48, pp.2603-2612, 2010.

[6] A. F. H. Goetz, B. C. Kindel, M. Ferri, and Z. Qu, "HATCH: results from simulated radiances, AVIRIS and Hyperion", *IEEE TGRS*, vol. 41, pp.1215-1221, 2003.

[7] M.S. Stefanou and J. P. Kerekes, "A method for assessing spectral image utility" *IEEE TGRS*, vol. 47, pp.1698-1706, 2009.

[8] S. G. Ungar, J. S. Pearlman, J. Mendenhall, and D. Reuter, "Overview of the Earth Observing 1 (EO-1) mission", *IEEE TGRS*, vol. 41, pp.1149-1159, 2003.

[9] L. Guanter, K. Segl, and H. Kaufmann, "Simulation of optical remote sensing scenes with application to the EnMAP hyperspectral mission", *IEEE TGRS*, vol. 47, pp.2340-2351, 2009.

[10] Kayser-Threde (http://www.kayser-threde.de).

[11] S. Delwart, R. Preusker, L. Bourg, R. Santer, D. Ramon, and J. Fischer, "MERIS in-flight spectral calibration", *Int. J. Remote Sens.*, vol. 28, pp.479-496, 2007.

[12] K.I. Itten, F. Dell'Endice, A. Hueni, M. Kneubühler, D. Schläpfer, D. Odermatt, F. Seidel, S. Huber, J. Schopfer, and T. Kellenberger, "APEX-the Hyperspectral ESA Airborne Prism Experiment", *Sensors*, vol. 10, pp.6235-6259, 2008.

[13] A. Hueni, J. Biesemans, K. Meuleman, F. Dell'Endice, D. Schläpfer, D. Odermatt, M. Kneubühler, S. Adriaensen, S. Kempenaers, J. Nieke, and K. I. Itten, "Structure, components, and interfaces of the Airborne Prism Experiment (APEX) processing and archiving facility", *IEEE TGRS*, vol. 47, pp.29-43, 2009.

[14] B.-C. Gao, M. J. Montes, and C. O. Davis, "Refinement of wavelength calibrations of hyperspectral imaging data using a spectrum-matching technique", *Remote Sensing Environ.*, vol. 90, pp.424-433, 2004.

[15] R.A. Neville, L. Sun, and K. Staenz, "Spectral calibration of imaging spectrometers by atmospheric absorption feature matching" *Can. J. Remote Sens.*, vol. 34 suppl. 1, pp. S29-S42, 2008.

[16] R. Richter, "A fast atmospheric correction algorithm applied to Landsat TM images", *Int. J. Remote Sens.*, pp. 159-166, 1990.

[17] K. Staenz and D. J. Williams, "Retrieval of surface reflectance from hyperspectral data using a look-up table approach", *Can. J. Remote Sens.*, vol. 23, pp. 354-368, 1997.

[18] S. M. Adler-Golden, M. W. Matthew, L. S. Bernstein et al., "Atmospheric correction for short-wave spectral imagery based on MODTRAN4", SPIE vol. 3753, pp.61-69, 1999.

[19] C. Miesch, L. Poutier, V. Achard, X. Briottet, X. Lenot, and Y. Boucher, "Direct and inverse radiative transfer solutions for visible and near-infrared hyperspectral imagery", *IEEE TGRS*, vol. 43, pp.1552-1562, 2005.

[20] R. Richter and D. Schläpfer, "Considerations on water vapor and surface reflectance retrievals for a spaceborne imaging spectrometer", *IEEE TGRS*, vol. 46, pp.1958-1966, 2008.

[21] L. Guanter, R. Richter, and H. Kaufmann, "On the application of the MODTRAN4 atmospheric radiative transfer code to optical remote sensing" *Int. J. Remote Sens.*, pp. 1407-1424, 2009.

[22] B.-C. Gao, M. J. Montes, C. O. Davis, and A. F. H. Goetz, "Atmospheric correction algorithms for hyperspectral remote sensing data of land and ocean", *Remote Sensing Environ.*, vol. 113, pp.S17-S24, 2009.

[23] A. Berk, L.S. Bernstein, G.P. Anderson, P.K. Acharya, D.C. Robertson, J.H. Chetwynd, and S.M. Adler-Golden, "MODTRAN cloud and multiple scattering upgrades with application to AVIRIS", *Remote Sens. Environ.*, vol. 65, pp. 367-375, 1998.

[24] A. Berk, G. P. Anderson, P. K. Acharya, M. L. Hoke, J. H. Chetwynd, L. S. Bernstein, E. P. Shettle, M. W. Matthew, and S. M. Adler-Golden, *MODTRAN4 Version 3 Revision 1 User's Manual*, Hanscom Air Force Base, MA: Air Force Res. Lab., 2003.

12

[25] R. Richter, "Correction of satellite imagery over mountainous terrain", *Appl. Opt.*, pp. 4004-4015, 1998.

[26] R. Richter, and D. Schläpfer, "Geo-atmospheric processing of airborne imaging spectrometry data. Part 2: atmospheric / topographic correction.", *Int. J. Remote Sens.*, vol. 23, pp. 2631-2649, 2002.

[27] D. Schläpfer, C.C. Borel, J. Keller, and K.I. Itten, "Atmospheric precorrected differential absorption technique to retrieve columnar water vapor", *Remote Sens. Environ.*, vol. 65, pp. 353-366 1998.

[28] Kayser-Threde, Munich, Germany, internal report 2008.

[29] L. Guanter, R. Richter, and J. Moreno, "Spectral calibration of hyperspectral imagery using atmospheric absorption features", *Applied Optics*, vol. 45, pp.2360-2370, 2006.

[30] J. S. Pearlman, P. S. Barry, C. C. Segal, J. Shepanski, D. Beiso, and S. L. Carman, "Hyperion, a space-based imaging spectrometer", *IEEE TGRS*, vol. 41, pp.1160-1173, 2003.

13

LIST OF TABLES

14

LIST OF FIGURES

15

TABLE I

Type of processing	Relative execution time
no smile correction	1
optimized smile correction for all channels	6
optimized smile correction, 118 absorption channels	4.2
brute force smile correction for all channels	66

TABLE II

ATMOSPHERIC SPECTRAL FEATURES SUITED FOR INFLIGHT CALIBRATION OF HIGH RESOLUTION IMAGING SPECTROMETERS. (MATCHING

RANGE = SPECTRAL RANGE OF ABSORPTION FEATURE INCLUDING LINE TAIL. WIDTH = DOMINATING PART OF ABSORPTION FEATURE).

Position	Type	Matching range	Width	Remarks
429 nm	Fraunhofer Lines	420-445	6 nm	narrow
517 nm	Fraunhofer Lines	500-540	8 nm	narrow
762 nm	Oxygen A	744-784	7 nm	stable
820 nm	Water Vapor	805-835	20 nm	stable
940 nm	Water Vapor	900-970	50 nm	broad feature
1130 nm	Water Vapor	1100-1170	60 nm	broad feature
1268 nm	Oxygen	1255-1285	12 nm	stable
1470 nm	Water Vapor	1450-1490	20 nm	in slope of absorption
2004 nm	CO_2	1985-2030	30 nm	double feature
2055 nm	CO_2	2040-2080	33 nm	double feature
2317 nm	Water Vapor/CH_4	2300-2330	20 nm	combined feature
2420 nm	Water Vapor	2400-2435	15 nm	in slope of absorption

TABLE III

GRID POINT POSITIONS IN THE LUT FOR THE 6 INPUT VARIABLES. CWV VALUES ARE GIVEN FOR SEA LEVEL GEOMETRY.

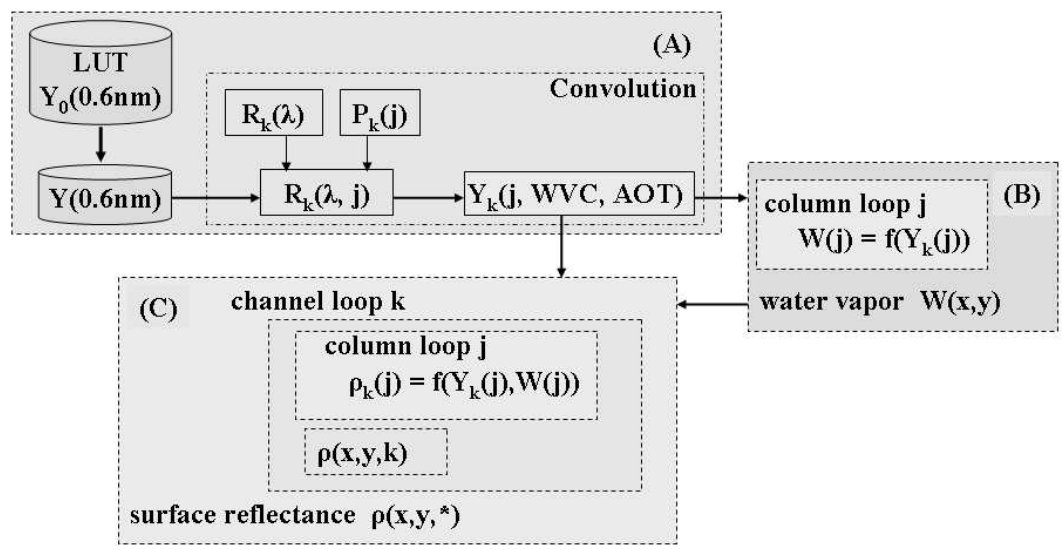|	#1	#2	#3	#4	#5	#6	#7	#8
VZA (°)	0	10	20	30				
SZA (°)	0	10	20	30	40	50	60	70
RAA (°)	0	30	60	90	120	150	180	–
ELEV (km)	0	0.7	1.5	2.5	–	–	–	–
VIS (km)	5	7	10	15	23	40	80	120
CWV (cm)	0.4	1	2	2.9	4	5	–	–

16

Fig. 1.　Schematic of optimized smile processor.

17

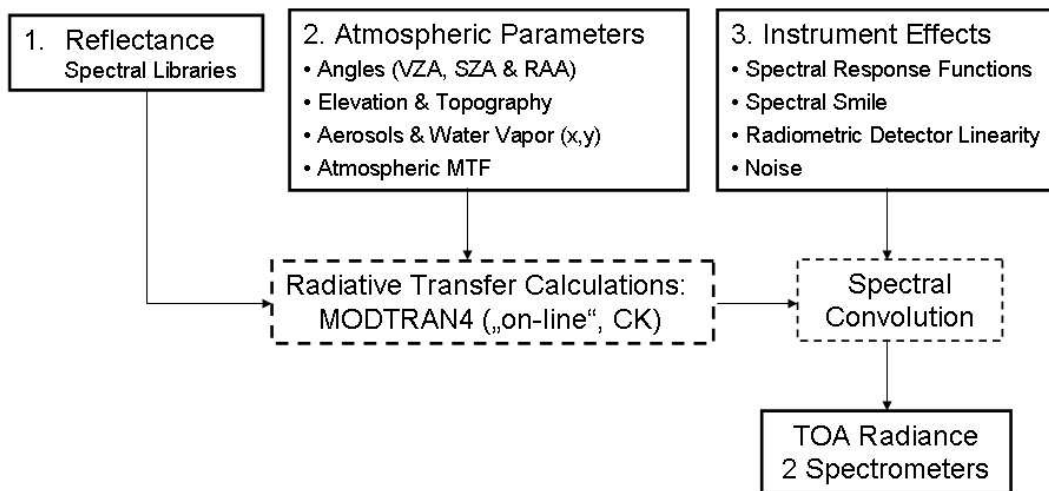Fig. 2.   Elements of the DLR hyperspectral simulator.
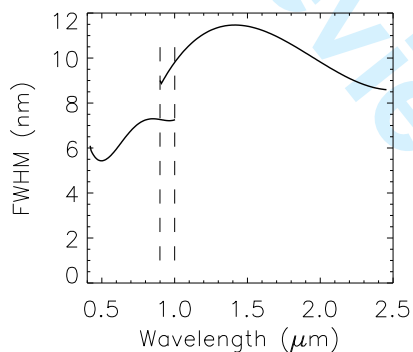
Fig. 3.   Bandwidth (FWHM) for both spectrometers of EnMAP.
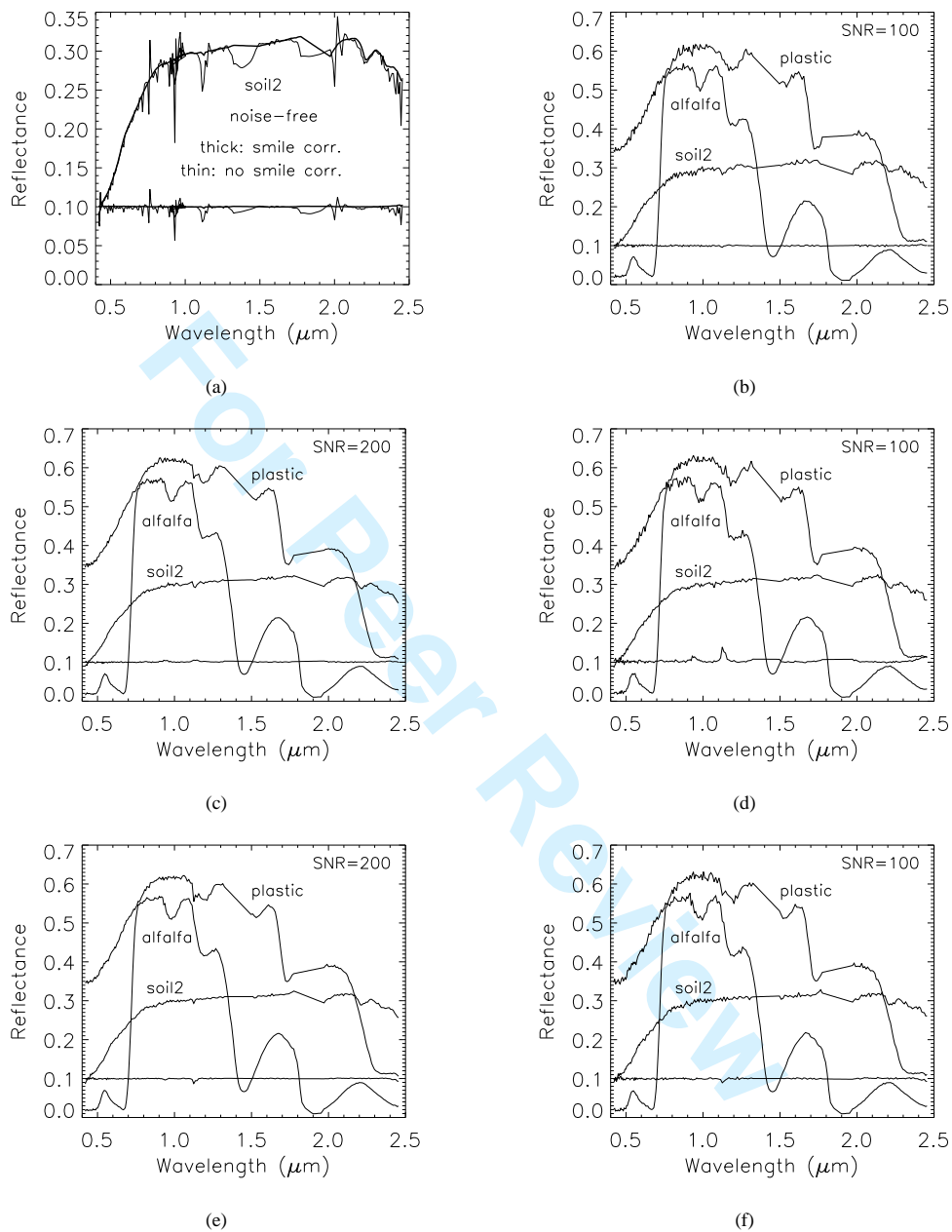
18

Fig. 4.   Results of selected reflectance retrievals. (a, b) SZA=35.5°, WVC=2.3 cm, (c, d) SZA=58°, WVC=3.8 cm, (e, f) SZA=58°, WVC=4.5 cm. The straight line with reflectance 0.1 represents a spectrally flat dark material.
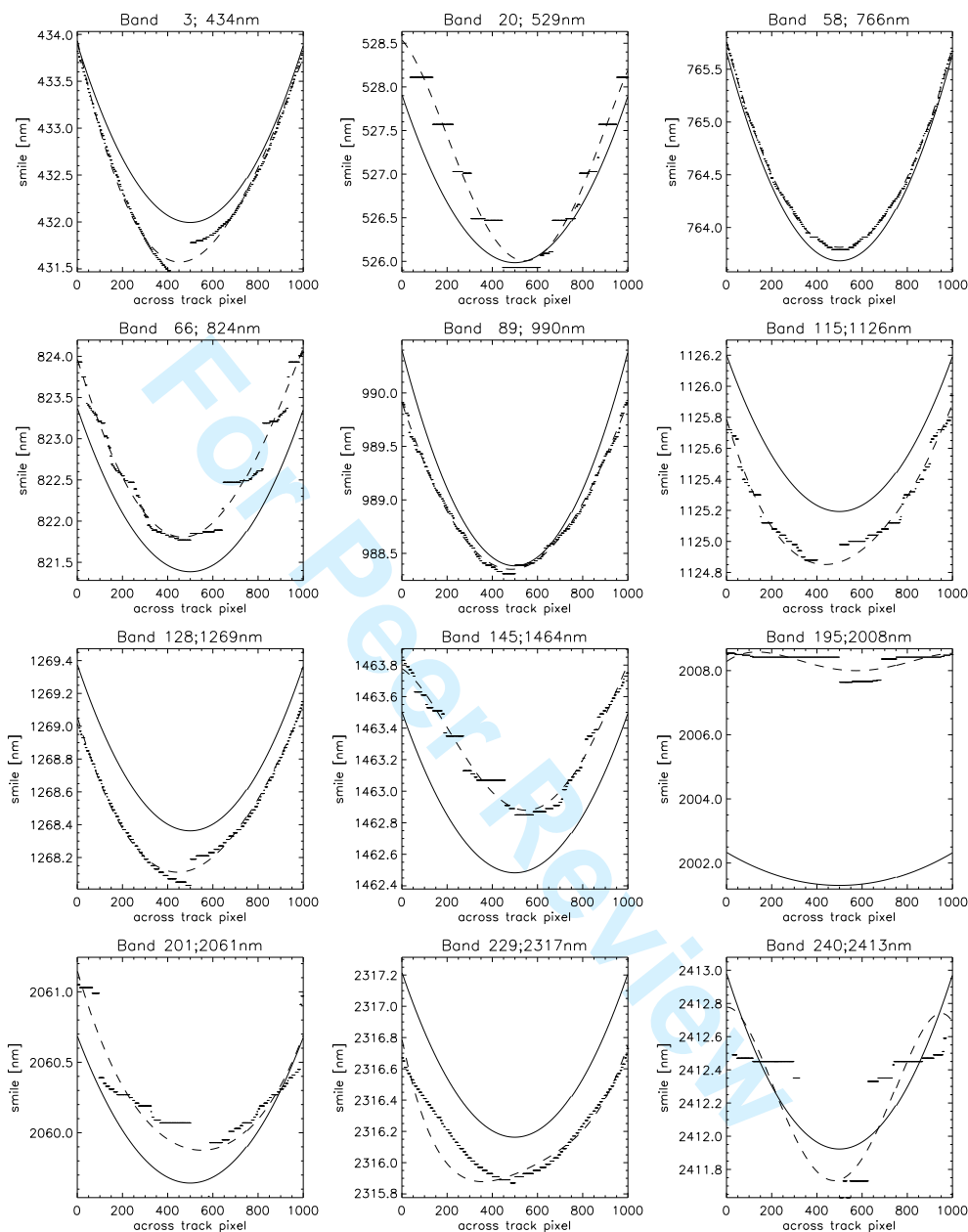
19

Fig. 5.   Image-based smile retrieval in comparison to the original smile data. Thick line: original smile function, dashed interpolation line: retrieved smile function, dots/horizontal lines: spectral position of best fit per image column.

20

no smile correction

columnar smile correction

linearly interpolated smile

smile and empirical vegetation correction

alfalfa   conifer
soil 1   soil 2
soil 3   polyethylene
albedo 0.1   albedo 0.2
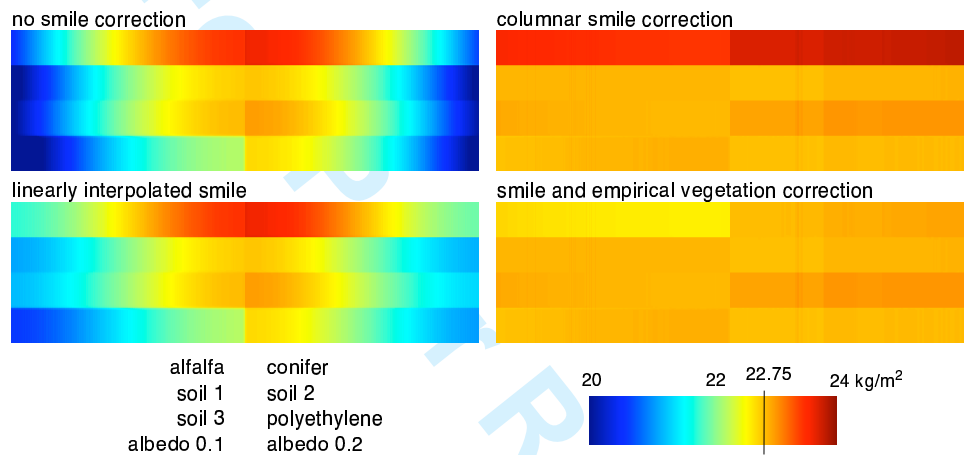
20   22   22.75   24 kg/m²

Fig. 6.   Results of four water vapor retrieval methods for a synthetic scene with eight surface types. The simulated constant water vapor column is 2.275 cm. Smile is simulated in the across-track direction (horizontal dimension in images).
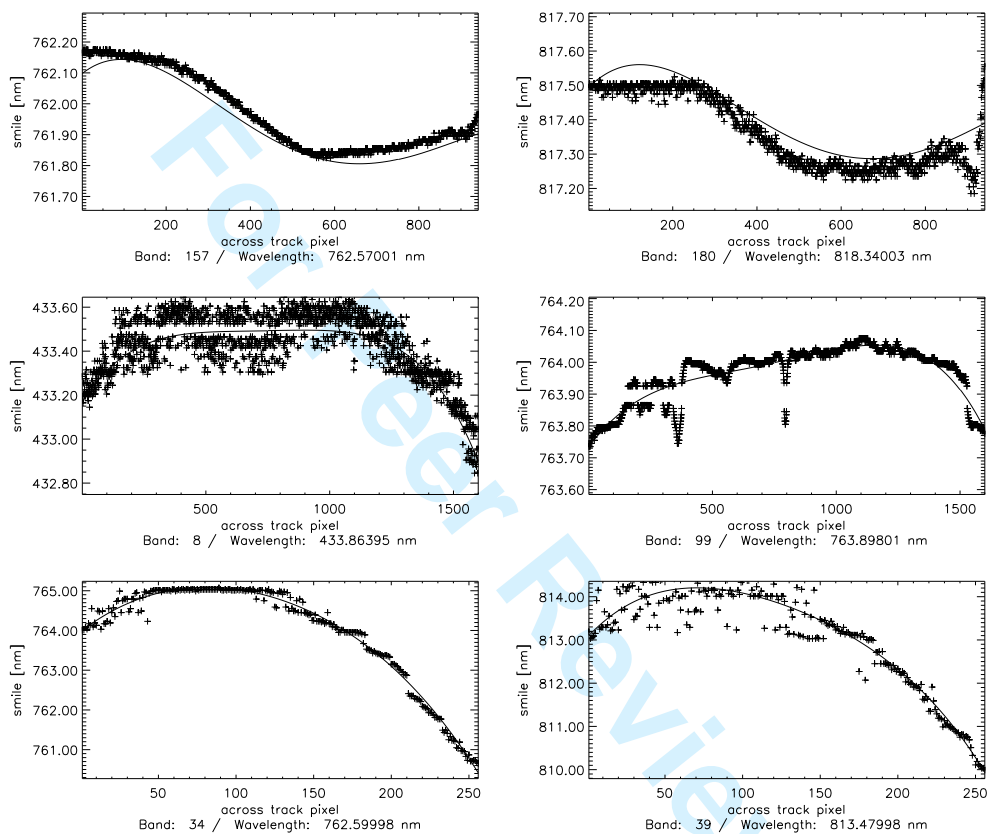
21

Fig. 7.   Selected image-based inflight smile retrieval results on standard images from AISA (top), HySpex (middle), and Hyperion (bottom).
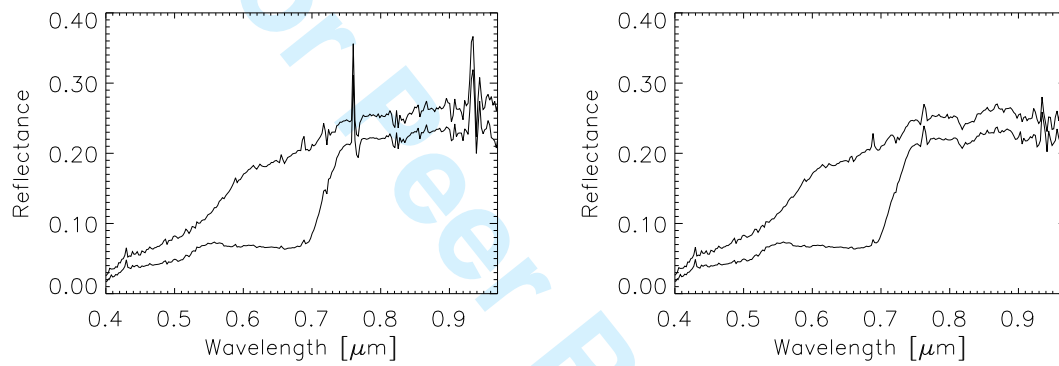
22

Fig. 8.   Atmospheric correction results for the AISA Eagle system, spectra without (left) and with (right) consideration of the smile effect. The spectral non-uniformity has been retrieved from the image. Remaining uncertainties are due to slight radiometric uncertainties.